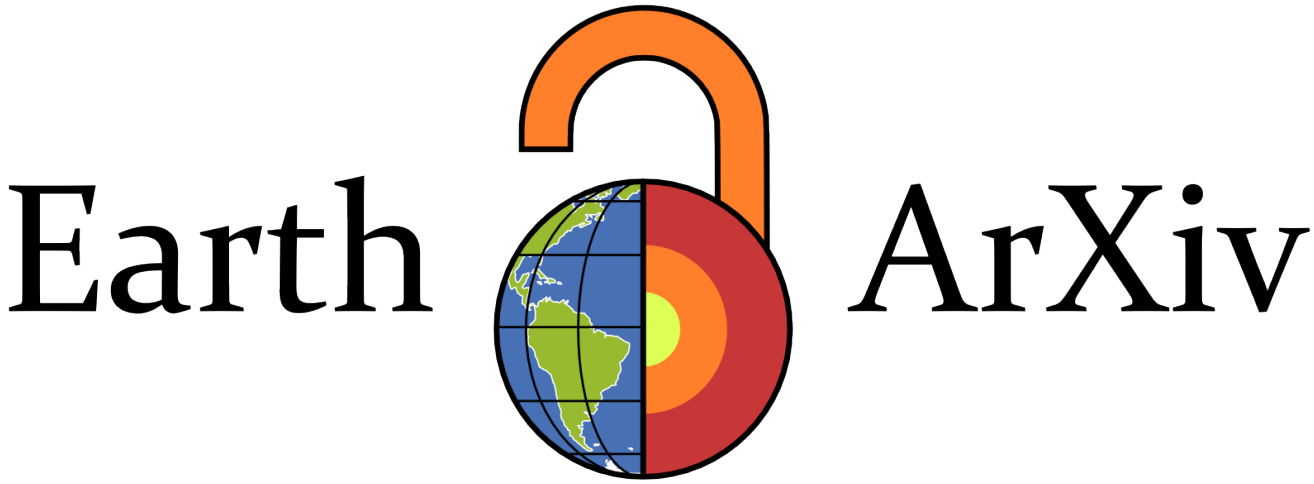

This manuscript has been submitted for publication in Seismological Research Letters (SRL). Please note that the manuscript has not yet been accepted for publication. Subsequent versions of this manuscript may have slightly different content. If accepted, the final version of this manuscript will be available via the 'Peer-reviewed Publication DOI' link on the right-hand side of this webpage.

Estimating the ice thickness and water depth of a frozen lake using flexural waves recorded by distributed acoustic sensing

Eduardo Valero Cano[*1], Ludovic Moreau[2], Felix Strobel[1], and Gregor Hillers[1]

Abstract

Information about frozen lakes, including ice rigidity, ice thickness, and water depth, is essential for both environmental studies and practical applications. Although these properties can be measured in the field, such measurements are labor-intensive and spatially limited, motivating the development of alternative observation methods. Seismic waves offer an alternative approach to studying frozen lakes, as their propagation velocity depends on the physical properties of the ice-water system, including the elastic moduli and thickness of the ice, and water column depth. In this study, we investigate the use of wind-driven flexural waves recorded by a distributed acoustic sensing (DAS) system to infer ice thickness and water depth under a 1000 m fiber-optic cable installed on Lake Pääjärvi, Finland. To do so, we identify wind-induced flexural waves in the 0.01-0.5 Hz frequency band, extract their dispersion curves, and invert them using a grid search to estimate effective ice thickness and water depth under four cable intervals. Our estimates reproduce the observed dispersion curves and agree with independent field measurements, demonstrating that it is possible to obtain first-order information about ice thickness and water depth in frozen lakes. However, the reliability of water depth estimates is limited by the wavenumber content of the flexural waves. In our case, water depth estimates become less robust with increasing water depth because low-wavenumber flexural waves, which are sensitive to the water column, are lacking. Another important observation is that refraction of flexural waves toward shallower water must be considered when converting apparent velocities measured along the cable to true velocities. If this effect is neglected, dispersion curves and the estimated parameters may be biased.

Introduction

Frozen lakes play a significant role in environmental processes, including methane trapping and climate-change monitoring (Langer et al., 2015; Mu et al., 2025), as well as in human activities, including ice-road transportation and recreation (Squire et al., 1988). Information on frozen lakes, namely ice rigidity, ice thickness, and water depth, is therefore required for both environmental studies and practical applications. Although the ice cover and water column can be sampled in the field, such measurements are labor-intensive and spatially limited, motivating the development of alternative observation methods.

Forces acting on lake ice generate seismic waves that propagate through the ice-water system. The propagation velocity of these waves depends on the physical properties of the ice-water system, including the elastic moduli and thickness of the ice and water column depth (Squire et al., 1996). As a result, seismic observations provide an alternative to direct field measurements for studying frozen lakes. For example, Moreau et al. (2020) inferred the thickness and elastic parameters of the Vallunden Lake ice cover using seismic waves generated by active sources and recorded by a geophone array. Similarly, Xie et al. (2024) estimated the Young's modulus of lake ice in Gansu Province, China, using seismic waves generated by icequakes and recorded by a distributed acoustic sensing (DAS) system.

While multiple studies exploit seismic waves generated by active sources or icequakes (Hunkins, 1960; Moreau et al., 2020, 2023; Xie et al., 2024; Quinn et al., 2025), relatively few exploit seismic waves generated by wind forcing. Studies such as Johnson et al. (2021) and Nziengui-Bâ et al. (2023) report observations of wind-driven flexural waves and demonstrate their use in estimating ice thickness and elastic properties. However, the robustness and practical limitations of estimates derived from wind-driven flexural waves still require investigation.

In this study, we investigate the use of wind-driven flexural waves recorded by a DAS system to infer the ice thickness and water depth under a 1000 m fiber-optic cable installed on Lake Pääjärvi, Finland. To do so, we identify flexural waves induced by the wind with the support of wind measurements obtained from nearby meteorological stations. Then, we measure dispersion curves of flexural waves along multiple cable intervals and invert them using a grid search to estimate effective values of ice thickness and water depth. By comparing these estimates with field measurements of ice thickness and water depth, we assess the accuracy of our estimates and comment on parameter uncertainty and trade-offs.

We begin this paper with an overview of seismic waves in ice plates and the dispersion of flexural waves. We then describe the DAS data and field measurements of ice thickness, water depth, and wind. Following the data description, we detail the identification and denoising of wind-driven flexural waves, as well as the measurement of dispersion curves. Finally, we describe the estimation of ice thickness and water depth, present and discuss the results, and draw conclusions.

1. Institute of Seismology, University of Helsinki, Helsinki, Finland, https://orcid.org/0000-0002-1294-0011 (EVC) https://orcid.org/0009-0005-4145-3043 (FS) https://orcid.org/0000-0003-2341-1892 (GH); 2. Institut des Sciences de la Terre, Université Grenoble Alpes, Grenoble, France, https://orcid.org/0000-0002-4381-9003 (LM)

*Corresponding author: eduardo.valerocano@helsinki.fi

Overview of seismic waves in ice plates

An ice plate floating on water acts as a waveguide. The high elastic-impedance contrast at the air-ice interface, together with the coupling of elastic plate modes in the ice with acoustic waves in the water, enable the propagation of guided modes (Squire et al., 1996). The energy distribution of these modes is determined by the product of the wavefield frequency and ice thickness. When this product is less than 50 Hz·m, most of the energy is concentrated in the fundamental quasi-symmetric (QS_0), fundamental shear-horizontal (SH_0), and quasi-Scholte (QS) modes (Moreau et al., 2020). In this regime, the QS_0 mode propagates as an axial wave, while the QS mode propagates as a flexural wave (Stein et al., 1998).

Each wave type dominates a particular displacement component. Axial waves dominate the radial component, shear-horizontal waves dominate the transverse component, and flexural waves dominate the vertical component, with weaker contributions to the radial component. Additionally, each wave type propagates at a different velocity, determined by distinct physical parameters of the ice-water system. The velocities of axial waves and low-frequency shear-horizontal waves are frequency-independent and determined by the density, Poisson's ratio, and Young's modulus of the ice (Squire et al., 1996). In contrast, the velocity of flexural waves varies with frequency and depends on additional parameters, as dictated by the dispersion relation of the QS mode (Squire et al., 1996; Romeyn et al., 2021).

The dispersion relation of the QS mode for a homogeneous, isotropic ice plate of thickness h floating on a water column of depth H is given by (Squire et al., 1996; Romeyn et al., 2021):

$$D(h)\frac{k^5}{\rho_{\mathrm{w}}} + gk = \omega^2 \left[kh\frac{\rho_{\mathrm{w}}}{\rho} + \coth(kH) \right], \tag{1}$$

with

$$D(h) = \frac{Eh^3}{12(1-\nu^2)}, \tag{2}$$

where $D(h)$ indicates the ice bending rigidity, k denotes wavenumber, ρ_w is the water density, $g = 9.81$ m/s^2 is the Earth's gravitational acceleration, ω denotes frequency, ρ indicates the ice density, E is the ice Young's modulus, and ν is the ice Poisson's ratio.

The phase velocity of flexural waves is obtained from Equation 1 using $c = \omega/k$. As implied by Equation 1, the product of wavenumber and water depth controls the relative influence of the ice plate and water column on the phase velocity. When $kH \gg 1$, $\coth(kH) \approx 1$, and the phase velocity is mainly determined by the ice plate properties. In contrast, if $kH \ll 1$, $\coth(kH) \approx 1/kH$, and the phase velocity is strongly influenced by the water column depth. Consequently, phase velocity increases with ice thickness in the elastic regime and with water depth in the hydro-elastic regime.

Datasets

Our datasets comprise strain-rate waveforms recorded by a DAS system and field measurements of ice thickness, water depth, and wind. The strain-rate waveforms and ice thickness measurements were acquired as part of an environmental seismol-

ogy project that included ∼350 seismic sensors, a microphone, a radar survey, hydro-acoustic sounding, and geochemical sampling (Strobel et al., 2025). The DAS data constitute the basis of our main analysis, while field measurements serve to complement the analysis and corroborate results.

Strain-rate waveforms

Strain-rate waveforms were continuously recorded by a FEBUS A-1 interrogator connected to a 1000 m fiber-optic cable. Waveforms were recorded for 23 days starting on 13 February 2025 using a sampling rate of 2500 Hz and a gauge length of 10 m. Channel spacing was 9.6 m during the first seven days of recording and 2 m thereafter, resulting in 104 and 500 DAS channels, respectively. The geolocalization of the channels was guided by Global Navigation Satellite System (GNSS) measurements (Strobel et al., 2025). Figure 1 shows the DAS system, with the interrogator on the lake shore and the cable extending towards the lake in three linear segments of 400, 300, and 300 m length, oriented WE, SE, and NS, respectively. The first 50 m of the cable lay on the lake shore, resulting in weaker coupling than the rest of the cable.

Ice thickness

Ice thickness measurements were acquired by Strobel et al. (2025) during two periods: 9–13 February 2025 and 3–4 March 2025. Measurements were taken at 210 geophone locations across the lake that follow an aperiodic tiling pattern (Mordret and Grushin, 2025) with a median nearest neighbor distance of 188 m. For this, a hole was drilled through the ice, and a ruler with a hook resting against the ice-water interface was inserted. In this study, we analyze the ice thickness measurements from 3–4 March 2025, as they are closer in time to the analyzed strain-rate waveforms from 21 February 2025. As shown in Figures 1c and d, the ice thickness below the DAS cable ranges from 25 to 26 cm.

Water depth

We retrieve the bathymetry of Lake Pääjärvi from the Finnish Meteorological Institute (FMI) database (https://en.ilmatieteenlaitos.fi/download-observations). To obtain water-depth profiles under the DAS cable, we interpolate isobaths on a regular grid using linear interpolation. Figures 1b and d indicate that water depth along the cable is not uniform but varies from 0 m at the lake shore to 42 m at the cable end.

Wind measurements

We obtain wind direction and speed measurements from the Hämeenlinna Katinen (HK) and Asikkala Pulkkilanharju (AP) meteorological stations via the FMI database. The measurements span 13–26 February 2025, with a sampling rate of 10 minutes. The HK and AP stations are approximately 36 km to the west and 30 km to the north-east of Lake Pääjärvi, respectively. Although both stations are far from each other, Figure 2 shows that their measurements are correlated, suggesting that they also indicate wind conditions at Lake Pääjärvi.

Detection and denoising of flexural waves

As noted in Johnson et al. (2021), low-frequency flexural waves are often excited by wind forcing. With this in mind, we detect flexural waves using wind measurements from the HK and AP meteorological stations and denoise them for subsequent analysis.

Detection

We convert DAS waveforms from FEBUS format to miniSEED, downsample to 5 Hz, and compute spectrograms for each DAS channel using ObsPy tools (Beyreuther et al., 2010). Then, we manually inspect the spectrograms and wind measurements to detect similarities. Figure 2 shows spectrograms of waveforms recorded at 60 m from the interrogator together with wind measurements. According to this figure, there is positive correlation between waveform amplitude at low frequencies ($<$ 0.2 Hz) and wind speeds, especially those measured at the HK meteorological station. For example, waveform amplitude is particularly high on 15, 18, and 21 February 2025, which coincides with elevated ($>$ 5m/s) wind speeds.

Figure 3 displays DAS waveforms from 21 February 2025 in the 0.01–0.2 Hz frequency band. A sequence of waves repeating over several minutes is visible along the cable. These waves propagate from the end to the start of the cable with an almost linear moveout and approximately an apparent velocity of 10 m/s. Given the cable location (Figure 1), this propagation suggests that waves originate roughly from the south, consistent with the regional wind direction on that day (Figure 2a). The moveout changes around 250 m from the interrogator, and reflections from the lake shore appear. The wave amplitude decreases from the end to the start of the cable; however, it increases again around 250 m from the interrogator, suggesting wave amplification or cable coupling differences.

The product between the signal frequency and Lake Pääjärvi ice thickness (Figure 1) is well below 50 Hz·m, indicating that we could be observing axial, shear-horizontal, or flexural waves. The apparent velocity of the signals is too low for axial or shear-horizontal waves (Moreau et al., 2020), suggesting that the signals correspond to flexural waves. Additionally, the frequency content and apparent velocity of the observed signals are consistent with those reported in Nziengui-Bâ et al. (2023), which recorded flexural waves in lake ice using a DAS system. Considering this evidence and the correlation between signal amplitude and wind speed, we conclude that the observed signals are flexural waves driven by wind forcing.

Denoising

Inspection of DAS waveforms shows that flexural waves persist for hours, have a consistent apparent velocity, and propagate in a similar direction. However, their relatively high noise levels complicate the analysis. To address this difficulty, we detect flexural waves in the 0.01–0.2 Hz frequency band using template matching (Gibbons and Ringdal, 2006) and stack them to reduce incoherent noise. We only stack flexural waves recorded on 21 February 2025, as including additional days can deteriorate the stacking results due to phase differences caused by variations in the ice thickness. This particular day is selected because wind speed was high, resulting in multiple flexural waves.

We use a Tukey window to isolate the arrival marked by the green lines in Figure 3 and use the result as a template. Because flexural waves are often not coherent along the entire cable, we use template matching over cable intervals: A (50–222 m), B (224–396 m), C (406–694 m), and D (704–1000 m). These intervals record coherent flexural waves and exclude channels near the cable corners, which have high noise levels. For each cable interval, we cross-correlate the template with the waveforms recorded on 21 February 2025 on a per-channel basis and average the results. Then, we identify peaks in the averaged cross-correlations and extract flexural waves at the corresponding lags. After testing multiple correlation thresholds, we select a threshold of 0.2 to detect correlation peaks. Once flexural waves are extracted, we stack them in the frequency-wavenumber domain to facilitate the measurement of dispersion curves.

Analysis of flexural waves

The observed flexural waves are sensitive to the ice thickness and water depth under the DAS cable. To infer these parameters, we measure the flexural waves dispersion. Since DAS systems record axial strain along the cable and therefore measure apparent wavenumbers, we estimate the backazimuth of the flexural waves to obtain true wavenumbers.

Dispersion curves

We measure dispersion curves of the flexural waves in the frequency-wavenumber (FK) domain. For each cable interval, we compute the two-dimensional Fourier transform to obtain the FK spectrum. Then, we normalize the FK spectrum along the frequency axis and manually pick spectral ridges to extract dispersion curves.

Figure 4 shows the FK spectrum and dispersion curves obtained for cable intervals A–D. The dispersion curves cover a relatively narrow frequency band, which shifts towards higher frequencies from cable interval A to D. According to Equation 1, the frequency of flexural waves at a given wavelength increases with water depth. Given that water depth increases from cable interval A to D, the observed frequency shift can be attributed to water depth changes.

The dispersion curves range between the apparent wavenumbers 0.03 and 0.24 rad/m, corresponding to apparent wavelengths between 26 and 209 m. For a DAS system, the shortest measurable wavelength must be at least twice the channel spacing and exceed the gauge length, whereas the longest measurable wavelength is approximately the cable length (Kennett, 2022; Vantassel et al., 2022). In our case, the channel spacing is 2 m, the gauge length is 10 m, and the cable interval lengths range from 172 to 296 m. Therefore, the dispersion curves cover apparent wavenumbers within the assessable range of our DAS system.

Propagation direction

DAS systems measure apparent wavenumbers given by $k_a = k \cdot \cos(\theta)$, where θ is the incidence angle of a plane wave relative to the cable. To determine the incidence angle and recover true wavenumbers, it is necessary to estimate the backazimuth

of the incoming waves. Therefore, we estimate the backazimuth of the flexural waves using cross-correlation beamforming (Ruigrok et al., 2017) in the 0.05–0.45 Hz frequency band.

Figure 5 shows beamforming maps for cable intervals A–D and for the entire cable. The beamforming maps for individual cable intervals display a ridge perpendicular to the interval direction. As discussed in Ende and Ampuero (2021), this beamforming pattern occurs for linear cable segments and indicates a trade-off between slowness and backazimuth. In contrast, the beamforming map for the complete cable exhibits two ridges, intersecting around 97.3 s/km slowness and 165.1° backazimuth. These ridges correspond to cable intervals C and D (Figures 5c and d). The ridges associated with cable intervals A and B do not contribute to the beamforming map, suggesting that flexural waves propagate along these intervals with a different backazimuth.

Wavefield redirection may explain why the backazimuth of flexural waves changes for cable intervals A and B. According to Equation 1, the phase velocity of flexural waves decreases with decreasing water depth, causing them to refract towards the shore as they approach shallow water, similar to ocean surface waves (Dean and Dalrymple, 1991). To illustrate this, we use Equation 1 and the parameters in Table 1 to compute the phase velocity of 0.1 Hz flexural waves for an ice plate of 25 cm thickness floating on Lake Pääjärvi. As shown in Figure 6, phase velocity decreases towards the shore following the bathymetry, supporting the interpretation that flexural waves are refracted towards the shore.

Coincidentally, all cable intervals are approximately perpendicular to the velocity gradient in Figure 6, suggesting that flexural waves propagate nearly along the cable with a small incidence angle. Because beamforming can not constrain the backazimuth of flexural waves for cable intervals A and B, we assume that the apparent wavenumbers measured on these intervals approximate the true wavenumbers. In contrast, using a backazimuth of 165.1°, we determine that the incidence angles for intervals C and D are 30° and 15°, respectively.

Estimation of ice thickness and water depth

We estimate the ice thickness and water depth along the cable intervals from the observed dispersion curves using the dispersion relation of the QS mode given in Equation 1. As indicated in Table 1, we set the ice density to 910 kg/m^3 and the water density to 1000 kg/m^3, which represent typical values (Moreau et al., 2020,?). We set the ice Young's modulus to 8.68 GPa and the ice Poisson's ratio to 0.4, derived in Strobel et al. (2025) from the velocity of axial and shear-horizontal waves recorded on Lake Pääjärvi.

For each cable interval, we convert the corresponding dispersion curve from apparent wavenumber to phase velocity using $c = (\omega/k_a) \cdot \cos(\theta)$ and perform a grid search over ice thickness and water depth. We explore the parameter space with increments of 1 cm in ice thickness and 20 cm in water depth, which provides a balance between resolution and computational cost. For each trial model, we compute synthetic dispersion curves using Equation 1 and evaluate the L2 misfit between observed and synthetic dispersion curves. Finally, we select the estimated model as the one that minimizes the misfit.

Results

Figure 7 summarizes the grid-search results for each cable interval. The left panels show the misfit surfaces, with black dots indicating the average ice thickness and average water depth calculated from field measurements, and blue dots indicating the estimated values. Correspondingly, the right panels show the fit between the observed and synthetic phase-velocity dispersion curves.

The estimated water depths for intervals A–D are 0.8, 6.5, 14.5, and 31.75 m. These values reflect the increase in water depth from the shore toward the lake interior. However, they underestimate the average water depth by 1.2, 4.6, 10.3, and 8.65 m. The estimated ice thicknesses for intervals A–D are 34, 30, 22, and 26 cm. The estimates for intervals C and D are relatively close to the average ice thickness, with differences of 3.8 and 0.5 cm, respectively. Meanwhile, the estimates for intervals A and B overestimate the observed values by 8.6 and 4.2 cm. Despite these discrepancies, the inferred models reproduce the observed dispersion curves reasonably well, with misfits ranging from 1 to 10 $(\mathrm{m/s})^2$ depending on the cable interval.

The shape of the misfit surfaces varies across cable intervals, indicating differences in parameter uncertainty. For interval A, the misfit surface is narrow in water depth and elongated in ice thickness, whereas for interval D the opposite pattern is observed. This indicates that water depth is better constrained than ice thickness for interval A, while ice thickness is better constrained than water depth for interval D. In contrast, the misfit surfaces for intervals B and C are more isotropic, suggesting balanced uncertainty in both parameters. To quantify parameter uncertainty, we compute the standard deviation of models with misfits below 10 $(\mathrm{m/s})^2$, as these models provide an acceptable fit to the data. The parameter uncertainties are reported in the left panels of Figure 7.

Discussion

Ice thickness and water depth estimates

Our estimation method assumes an ice plate of uniform thickness and a water column of constant depth, assumptions that are not valid for Lake Pääjärvi. Therefore, the inferred parameters should be interpreted as effective ice thickness and water depth as sensed by flexural waves. Because the spatial sensitivity of flexural waves depends on their wavelength, these effective values reflect wavelength-dependent averaging and cannot be easily equated with the true ice thickness or water depth. Despite these caveats, our estimates are comparable to the arithmetic averages of field measurements, indicating that flexural waves can be used to obtain first-order estimates of ice thickness and water depth.

Relative sensitivity to ice thickness and water depth

The uncertainty of the estimates, particularly for water depth, varies across cable intervals, indicating that the observed dispersion curves resolve the parameters differently. According to Equation 1, flexural waves are more sensitive to the water column when the product of wavenumber and water depth is much less than one. Consequently, wavenumbers sensitive to the water column become progressively lower as the water depth increases. In our experiment, water depth increases from

cable interval A to D, whereas the lowest wavenumber resolved by the dispersion curves remains approximately constant. As a result, the dispersion curves become less sensitive to water depth, increasing the uncertainty of water depth estimates from cable intervals A to D.

Influence of flexural-wave incidence angle

Neglecting the incidence angle of flexural waves leads to an overestimation of their phase velocity. Because phase velocity tends to increase with increasing ice thickness and water depth, this can bias the estimated parameters toward higher values. In this study, we estimated the backazimuth of flexural waves and accounted for the incidence angle with respect to cable intervals C and D. For cable intervals A and B, however, we assumed that apparent wavenumbers approximate true wavenumbers due to refraction of the flexural waves. Consequently, phase velocity may be overestimated for these intervals, which can explain why the estimated ice thickness exceeds the average field measurements.

Conclusions

We investigated the use of wind-driven flexural waves recorded by a DAS system to infer the ice thickness and water depth along a 1000 m fiber-optic cable deployed on Lake Pääjärvi, Finland. Specifically, we measured phase-velocity dispersion curves of flexural waves and estimated the effective ice thickness and water depth under four cable intervals using a grid search. Our estimates reproduce the observed dispersion curves and agree with field measurements, demonstrating that it is possible to obtain first-order information about ice thickness and water depth on frozen lake systems. However, the reliability of water depth estimates is limited by the wavenumber content of the flexural waves. In our case, water depth estimates become less robust with increasing water depth because low-wavenumber flexural waves, which are sensitive to the depth of the water column, are lacking. Another important observation is that refraction of flexural waves toward shallower water must be considered when converting apparent velocities measured along the cable to true velocities. If this effect is neglected, dispersion curves and the estimated parameters can be biased. Overall, this study demonstrates that DAS observations of naturally excited low-frequency flexural waves provide an effective means to infer ice thickness and water depth in frozen lakes, while highlighting key factors that affect the reliability of the estimates.

Data and Resources

The data that support the findings of this study are available from the corresponding author upon request.

Declaration of Competing Interests

The authors acknowledge that there are no conflicts of interest recorded.

Acknowledgments

This work was supported by the Research Council of Finland (Academy project DYNALake–dynamics of a frozen lake environment grant 362968, and Flagship of Advanced Mathematics for Sensing Imaging and Modelling grant 359182).

References

Beyreuther, M., R. Barsch, L. Krischer, T. Megies, Y. Behr, and J. Wassermann (2010, 05). Obspy: A python toolbox for seismology. *Seismological Research Letters* **81**(3), 530–533.

Dean, R. G. and R. A. Dalrymple (1991). *Water wave mechanics for engineers and scientists*, Volume 2. world scientific publishing company.

Ende, M. P. V. D. and J. P. Ampuero (2021, 4). Evaluating seismic beamforming capabilities of distributed acoustic sensing arrays. *Solid Earth* **12**, 915–934.

Gibbons, S. J. and F. Ringdal (2006). The detection of low magnitude seismic events using array-based waveform correlation. *Geophysical Journal International* **165**(1), 149–166.

Hunkins, K. (1960, 10). Seismic studies of sea ice. *Journal of Geophysical Research* **65**, 3459–3472.

Johnson, M. A., A. V. Marchenko, D. O. Dammann, and A. R. Mahoney (2021). Observing wind-forced flexural-gravity waves in the beaufort sea and their relationship to sea ice mechanics. *Journal of Marine Science and Engineering* **9**(5).

Kennett, B. L. (2022). The seismic wavefield as seen by distributed acoustic sensing arrays: Local, regional and teleseismic sources. *Proceedings of the Royal Society A: Mathematical, Physical and Engineering Sciences* **478**.

Langer, M., S. Westermann, K. Walter Anthony, K. Wischnewski, and J. Boike (2015). Frozen ponds: production and storage of methane during the arctic winter in a lowland tundra landscape in northern siberia, lena river delta. *Biogeosciences* **12**(4), 977–990.

Mordret, A. and A. G. Grushin (2025, 3). Beating the aliasing limit with aperiodic monotile arrays. *Physical Review Applied* **23**.

Moreau, L., P. Boué, A. Serripierri, J. Weiss, D. Hollis, I. Pondaven, B. Vial, S. Garambois, Éric Larose, A. Helmstetter, L. Stehly, G. Hillers, and O. Gilbert (2020, 4). Sea ice thickness and elastic properties from the analysis of multimodal guided wave propagation measured with a passive seismic array. *Journal of Geophysical Research: Oceans* **125**.

Moreau, L., L. Seydoux, J. Weiss, and M. Campillo (2023, 3). Analysis of microseismicity in sea ice with deep learning and bayesian inference: Application to high-resolution thickness monitoring. *Cryosphere* **17**, 1327–1341.

Moreau, L., J. Weiss, and D. Marsan (2020). Accurate estimations of sea-ice thickness and elastic properties from seismic noise recorded with a minimal number of geophones: From thin landfast ice to thick pack ice accurate estimations of sea-ice thickness and elas-tic properties from seismic noise recorded with a minimal number of geophones: From thin landfast ice to thick pack ice. *Journal of Geophysical Research. Oceans* **125**, 2141–2167.

Mu, C., P. Lei, M. Mu, C. Zhang, Z. Zhou, J. Song, Y. Jia, C. Fan, X. Peng, G. Zhang, et al. (2025). Methane emissions from thermokarst lakes must emphasize the ice-melting impact on the tibetan plateau. *Nature Communications* **16**(1), 2404.

Nziengui-Bâ, D., O. Coutant, Moreau, and P. Boué (2023, 5). Measuring the thickness and young's modulus of the ice pack with das, a test case on a frozen mountain lake. *Geophysical Journal International* **233**, 1166–1177.

Quinn, M., A. K. Doran, C. Coclin, L. Cass, and H. Turner (2025, 6). Freshwater thin ice sheet monitoring and imaging with fiber optic distributed acoustic sensing. *Glacies* **2**, 7.

Romeyn, R., A. Hanssen, B. O. Ruud, and T. A. Johansen (2021, 6). Sea ice thickness from air-coupled flexural waves. *Cryosphere* **15**, 2939–2955.

Ruigrok, E., S. Gibbons, and K. Wapenaar (2017, 5). Cross-correlation beamforming. *Journal of Seismology* **21**, 495–508.

Squire, V., R. J. Hosking, A. D. Kerr, and P. Langhorne (1996). *Moving Loads on Ice Plates*. Dordrecht, The Netherlands: Kluwer Academic Publishers.

Squire, V. A., W. H. Robinsont, P. J. Langhorne, and T. G. Haskell (1988). Vehicles and aircraft on floating ice. Technical report.

Stein, P. J., S. E. Euerle, and J. C. Parinella (1998, 9). Inversion of pack ice elastic wave data to obtain ice physical properties. *Journal of Geophysical Research: Oceans* **103**, 21783–21793.

Strobel, F., E. Valero Cano, and G. Hillers (2025). Investigating a frozen lake using seismic waves: The dynalake project. In *Proceedings of the 13th National Seminar on Snow*, Oulu, Finland. 31 October 2025.

Vantassel, J. P., B. R. Cox, P. G. Hubbard, and M. Yust (2022, 10). Extracting high-resolution, multi-mode surface wave dispersion data from distributed acoustic sensing measurements using the multichannel analysis of surface waves. *Journal of Applied Geophysics* **205**.

Xie, J., X. Zeng, C. Liang, S. Ni, R. Chu, F. Bao, R. Lin, B. Chi, and H. Lv (2024, 2). Ice plate deformation and cracking revealed by an in situ-distributed acoustic sensing array. *Cryosphere* **18**, 837–847.

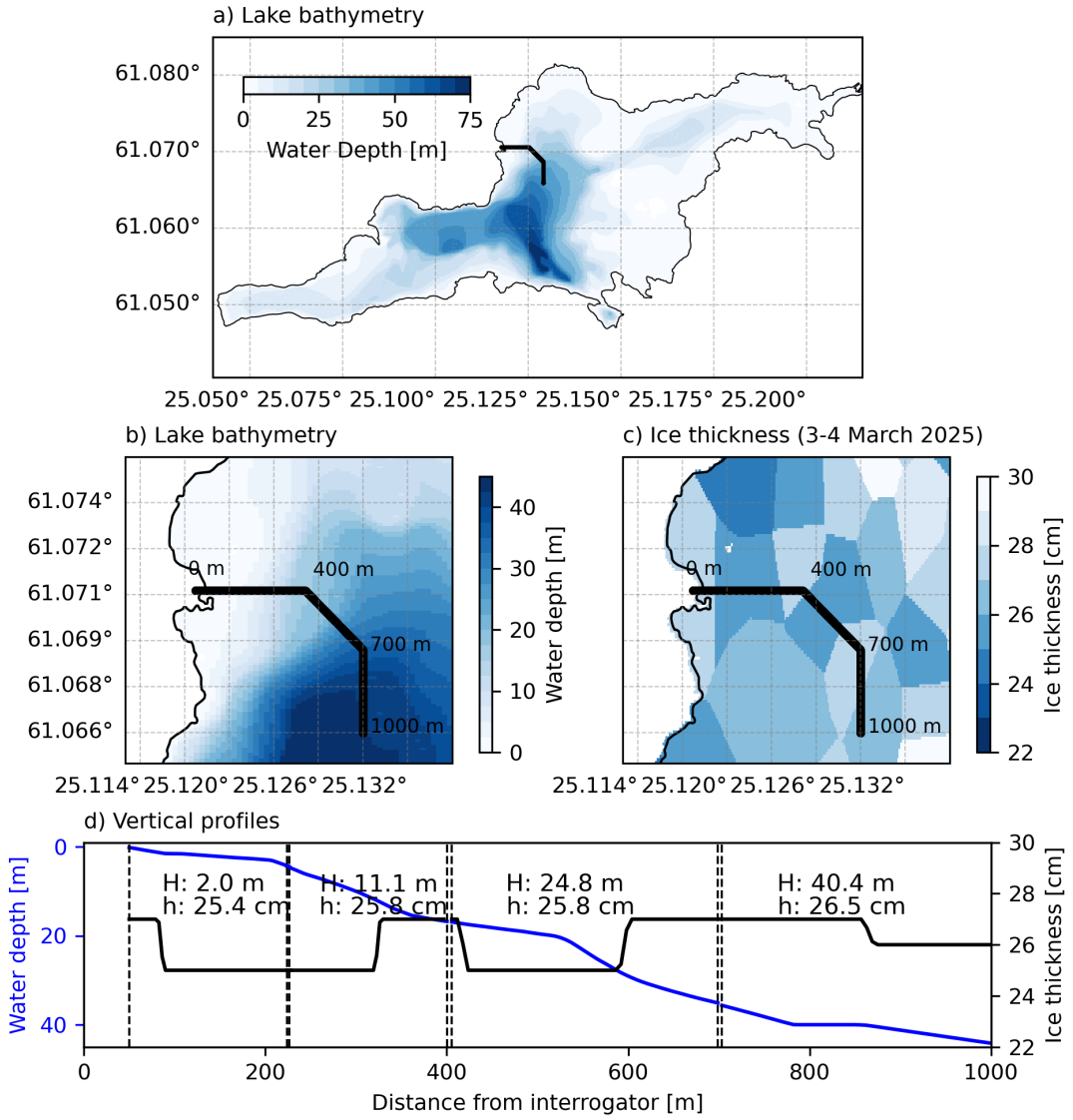

Figure 1. Bathymetry and ice thickness of the study area. (a) Lake Pääjärvi bathymetry. (b) Close-up view of panel a. (c) Lake Pääjärvi ice thickness measured on 3–4 March 2025. (d) Bathymetry (blue line) and ice thickness (black line) along the DAS cable. The black line in panels a–c indicates the DAS cable. Dotted black lines in panel d mark the boundaries of cable intervals A–D; H and h denote the average water depth and ice thickness of each interval, respectively.

290

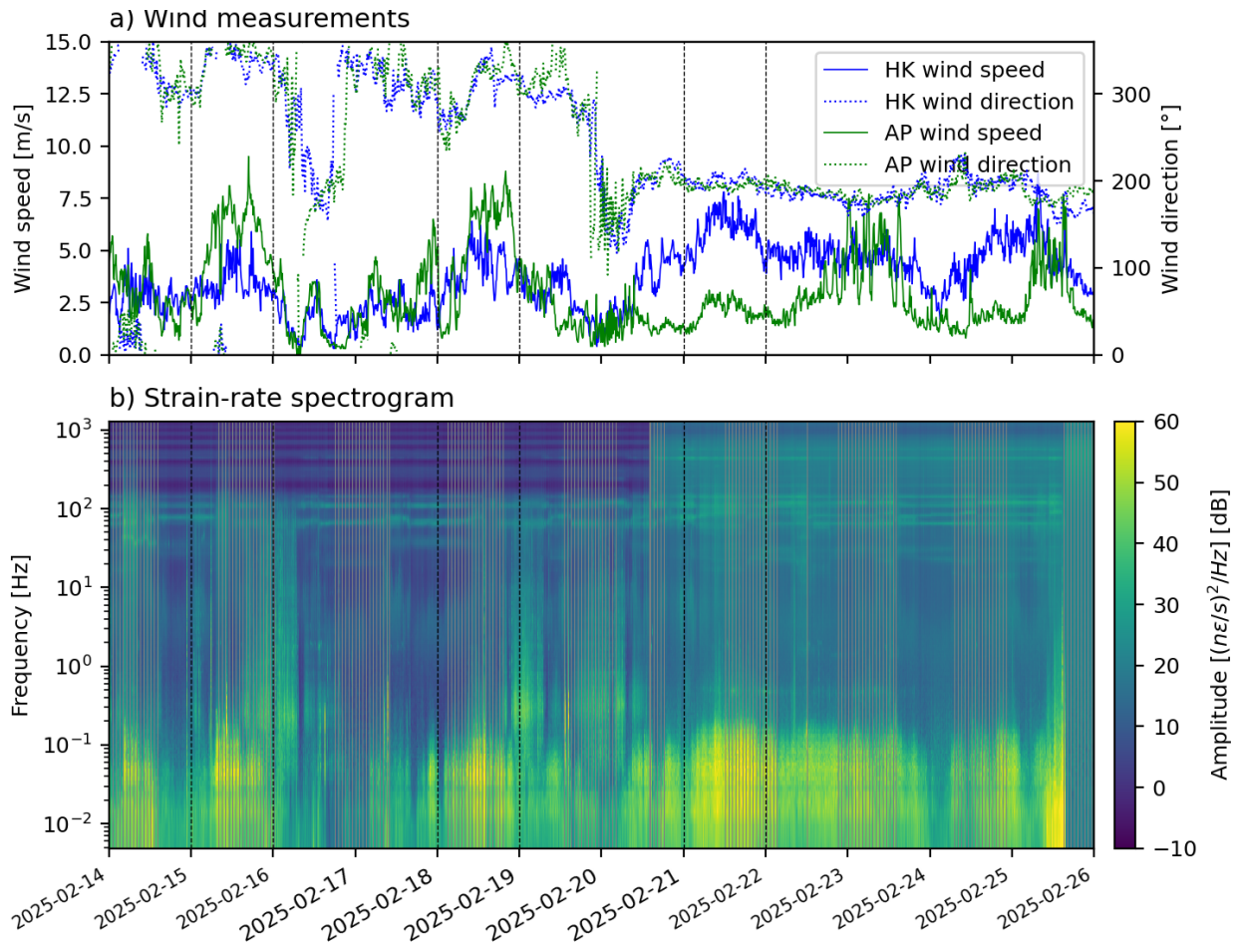

Figure 2. Wind measurements and spectrogram of DAS waveforms from 14-26 February 2025. (a) Wind speed (solid lines) and direction (dotted lines) measured at the Hämeenlinna Katinen (HK) and Asikkala Pulkkilanharju (AP) meteorological stations. (b) Spectrogram of strain rate recorded by at 60 m from the interrogator. The dotted black lines in panels a and b highlight days where wind speed correlates with signal amplitude.

TABLE 1.
Physical parameters used to model synthetic flexural wave dispersion curves.

Parameter	Value
Earth's gravitational acceleration g	9.81 $\mathrm{m/s^2}$
Ice density ρ	910 $\mathrm{kg/m^3}$
Ice Poisson's ratio ν	0.4
Ice Young's modulus E	8.68 GPa
Water density ρ_w	1000 $\mathrm{kg/m^3}$

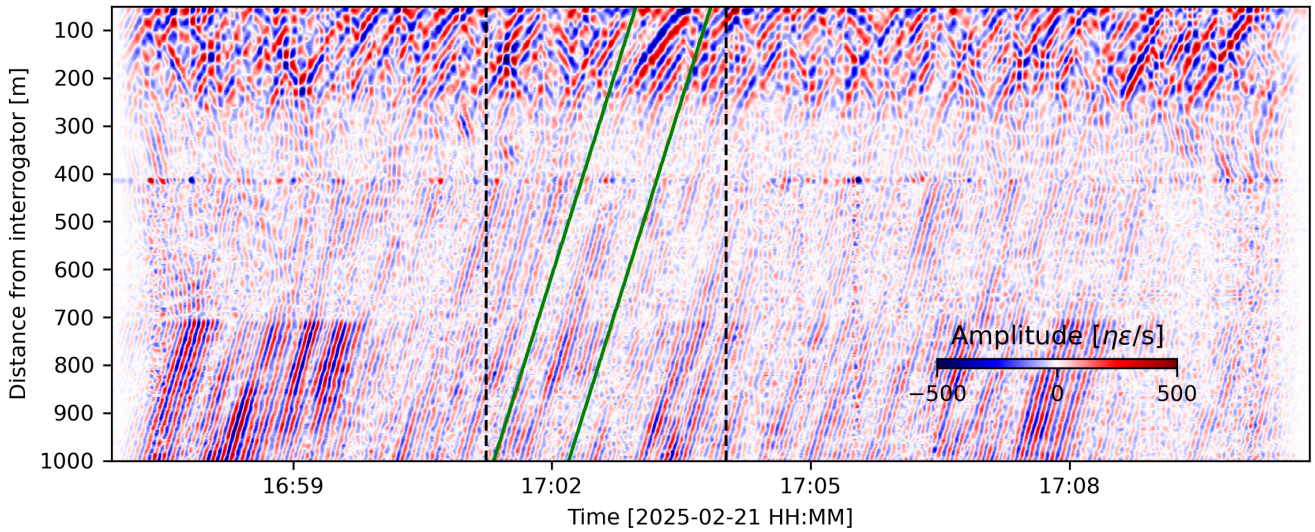

Figure 3. DAS waveforms recorded on 21 February 2025 filtered between 0.002-0.2 Hz. Incoming flexural waves are visible along the entire cable, while reflections from the lake shore are mainly observed between 50 and 400 m from the interrogator. Dotted black lines indicate the boundaries of the template-matching window, and green lines show the limits of the Tukey taper used to isolate the template.

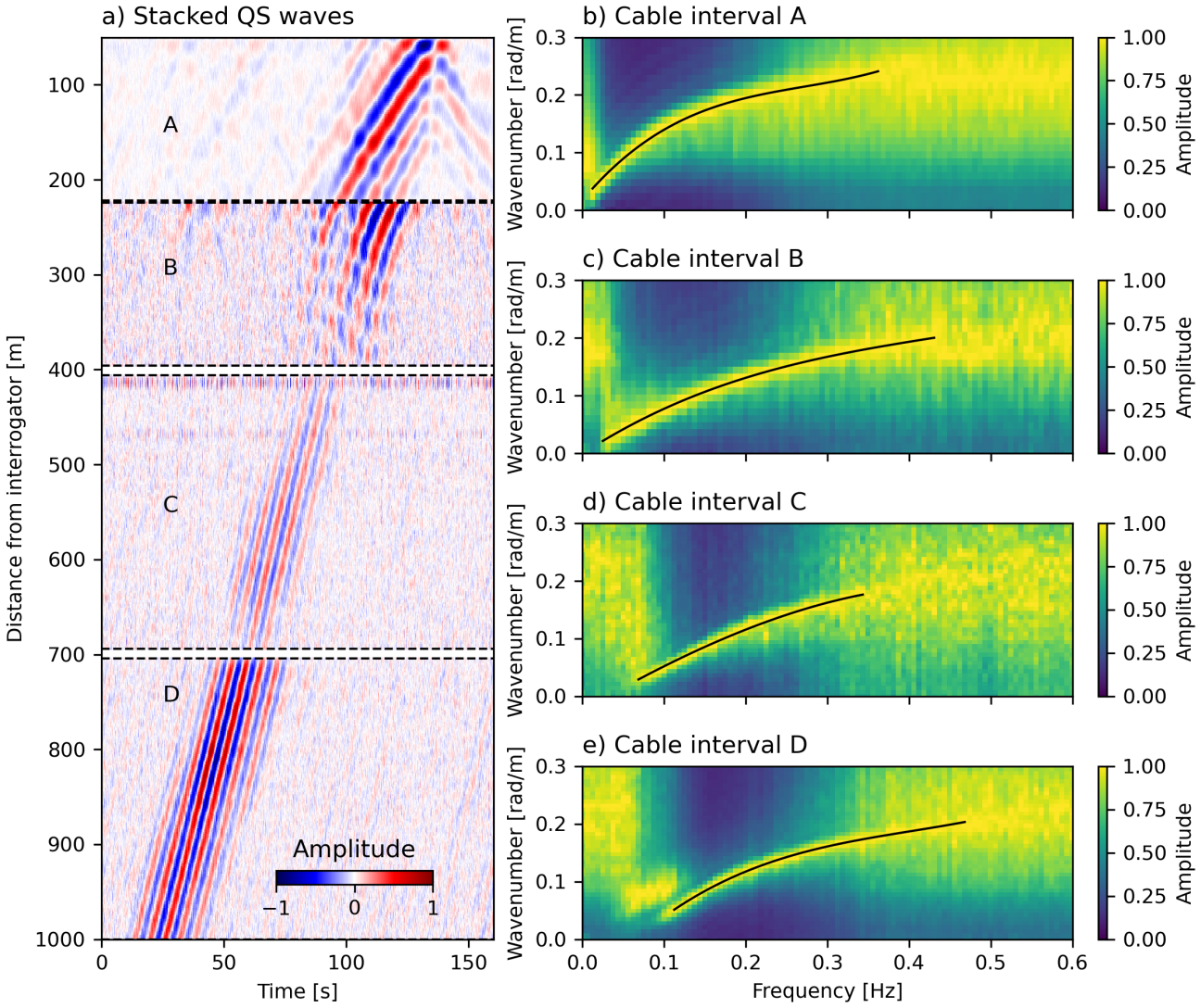

Figure 4. Flexural waves and dispersion measurements. (a) Unfiltered flexural waves. (b-e) FK spectrum for cable intervals A–D. Black lines in panels b–e show the measured apparent wavenumbers.

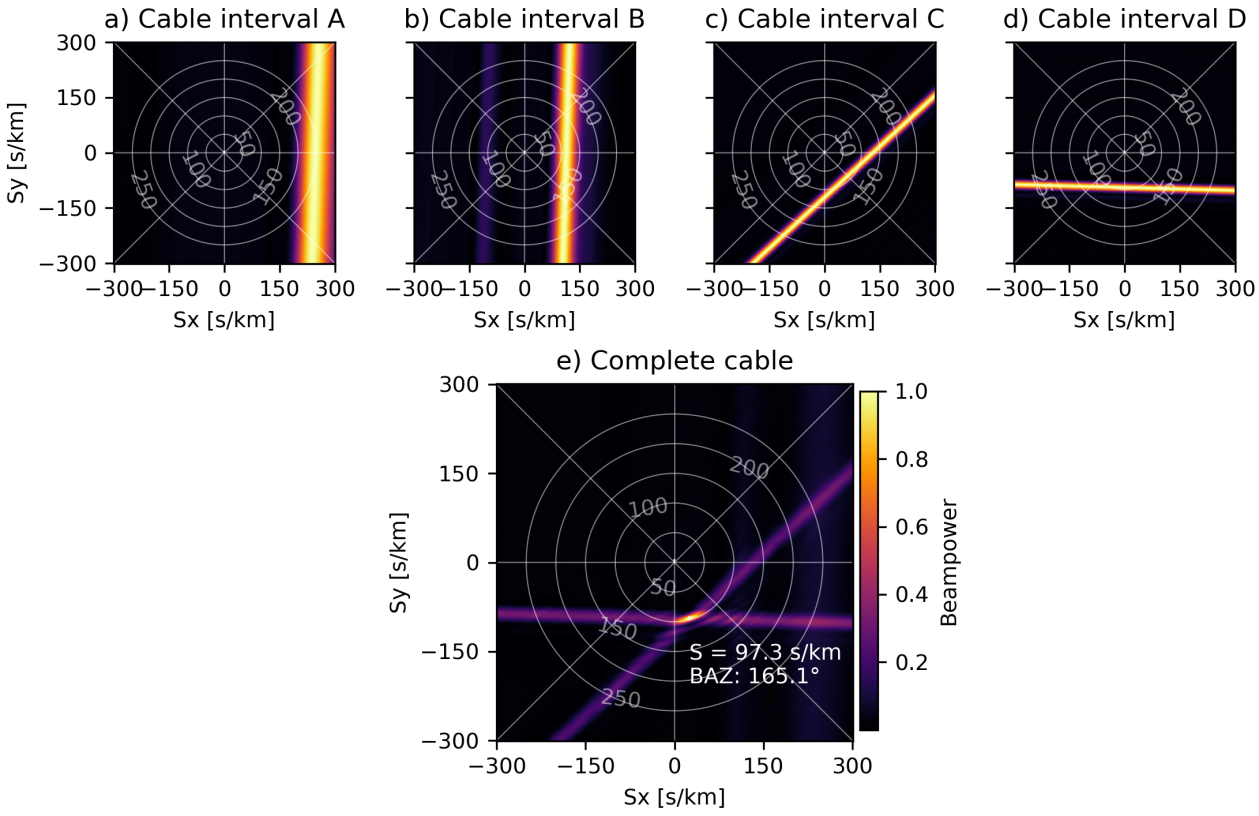

Figure 5. Beamforming of the flexural waves filtered between 0.05–0.45 Hz. (a-d) Beamforming results for cable intervals A–D. (e) Beamforming result for the complete cable. White contours indicate slowness in s/km. S and BAZ indicate the slowness and backazimuth of maximum beampower, respectively.

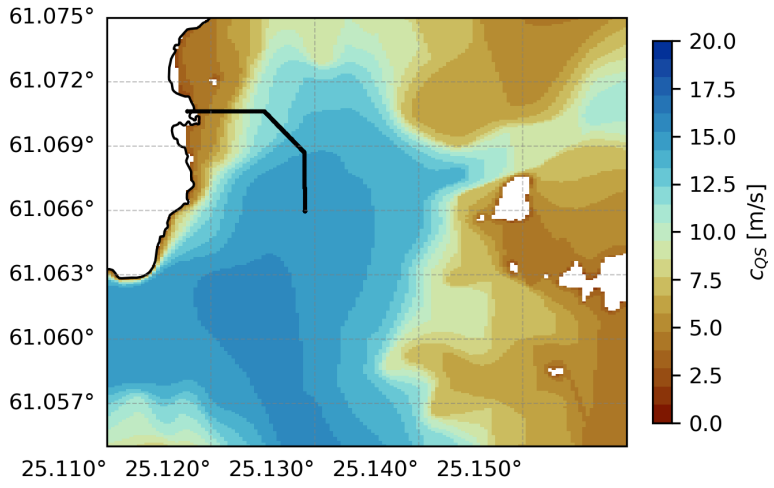

Figure 6. Theoretical velocity of flexural waves (c_{QS}) at 0.1 Hz for an ice plate of 25 cm thickness floating on the Lake Pääjärvi water column (Figure 1). The velocity is computed using Equation 1 and the physical properties specified in Table 1.

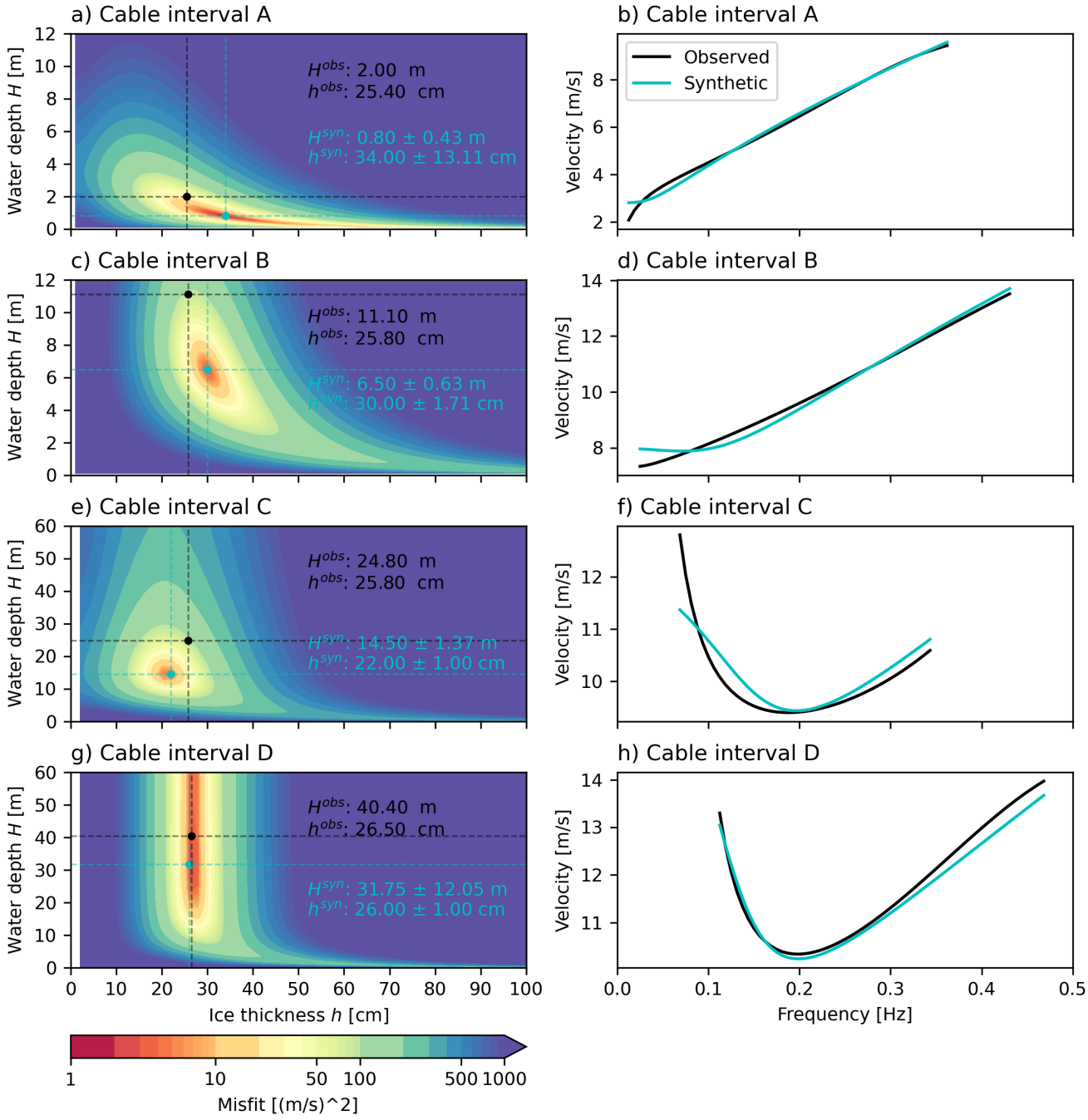

Figure 7. Estimation results and data fit for cable intervals A–D. Left panels: Grid-search misfit surfaces. Black and blue dots indicate observed and estimated values of water depth (H) and ice thickness (h), respectively. Reported standard deviations correspond to models with misfits below 10 $(\mathrm{m/s})^2$. Right panels: Comparison between observed (black) and synthetic (blue) flexural wave dispersion curves for the best-fit model.